# Rainfall Microphysics Influenced by Strong Wind during a Tornadic Storm

ABDULLAH BOLEK[a] AND FIRAT Y. TESTIK[a]

[a] *Civil and Environmental Engineering Department, The University of Texas at San Antonio, San Antonio, Texas*

(Manuscript received 9 January 2021, in final form 10 September 2021)

ABSTRACT: Rainfall microphysical characteristics including raindrop fall speed, axis ratio, and canting angle were measured through field observations by using a high-speed optical disdrometer (HOD) during and after tornadic severe storm passage. High and low wind and turbulence characteristics were observed during and after passage, respectively, which provided an opportunity to compare the effects of the different wind and turbulence characteristics on raindrop characteristics. During passage, 9.4% of the raindrops larger than 1.0 mm in volume equivalent diameter ($D$) were identified as subterminal, whereas only 0.5% of the raindrops of the same size were detected as subterminal after passage. Contrary to findings in literature, we could not find any distinct superterminal fall speed behavior for raindrops with $D < 1.0$ mm during or after passage. For raindrops with $D > 2.0$ mm, deviations of the axis ratio distribution from the predicted distribution for the equilibrium raindrops were observed, and the deviations during passage were larger than those after passage. The deviations of the axis ratio distributions from the predicted distributions for the equilibrium raindrops were also observed for midsized ($1.0 < D < 2.0$ mm) raindrops; however, these deviations during and after passage were of similar magnitude. The canting angle distribution for raindrops with $D > 2.0$ mm was found to have the mean value of approximately 0° both during and after passage and the standard deviation values of 24.7° during passage and 13.6° after passage. This study shows the clear influence of wind on various rainfall microphysical characteristics and documents the observed value ranges of these characteristics under strong wind that are of importance for a number of rainfall applications, including radar rainfall retrievals and rainfall modeling.

KEYWORDS: Rainfall; Hydrometeorology; Turbulence; Wind; Severe storms; Surface observations

## 1. Introduction

Microphysical characteristics of raindrops such as shape, fall velocity, and canting angle are important for many hydrological and agricultural applications such as radar- and ground-based rainfall rate estimations, soil erosion, water resources management, and urban hydrology (Testik and Barros 2007; Testik and Gebremichael 2010; Angulo-Martínez and Barros 2015). There have been various laboratory studies that have provided valuable information on raindrop characteristics (Gunn and Kinzer 1949; Pruppacher and Beard 1970; Beard et al. 1991; Beard and Kubesh 1991; Andsager et al. 1999). Raindrops are generally considered to fall through stagnant air at terminal speed with an equilibrium shape determined by the internal circulation, electrical stress, hydrostatic, aerodynamic, and surface tension forces (McDonald 1954; Beard and Chuang 1987, hereafter BC1987; Testik and Barros 2007). The equilibrium shapes of raindrops change from spherical to oblate spheroid as the raindrop diameter ($D$) increases (e.g., Pruppacher and Beard 1970). Several mathematical models were proposed to estimate the equilibrium raindrop shapes (Green 1975; Pruppacher and Pitter 1971; BC1987). In many applications, raindrop shape is represented using the raindrop axis ratio ($\alpha$), which is the ratio of the maximum vertical and maximum horizontal chords. Among the shape models, the BC1987 model has been widely used and verified (Andsager et al. 1999; Thurai and Bringi 2005; Thurai et al. 2007; Thurai and Bringi 2009; Chowdhury et al. 2016). A polynomial fit to BC1987 based on $D$ (in units of millimeters) as defined in Eq. (1) (Andsager et al. 1999) was used in this study to provide raindrop shape predictions for comparisons with our field observations:

$$\alpha = 1.0048 + 5.7 \times 10^{-4}(D) - 2.628 \times 10^{-2}(D^2) + 3.682 \times 10^{-3}(D^3) - 1.677 \times 10^{-4}(D^4). \quad (1)$$

Since Gunn and Kinzer's (1949) pioneering laboratory study on terminal speeds of water drops falling under calm laboratory conditions, researchers have conducted various laboratory and theoretical efforts to simulate raindrop fall in the laboratory environment (Beard and Pruppacher 1969; Beard 1976, 1977; Wang and Pruppacher 1977; Chowdhury et al. 2016) and to parameterize raindrop terminal speed (Best 1950; Foote and Du Toit 1969; Wobus et al. 1971; Dingle and Lee 1972; Atlas et al. 1973). Appendix A of Testik and Barros (2007) provides a comprehensive list of terminal speed parameterizations. Among these parameterizations, Atlas et al.'s (1973) parameterization, which is an empirical fit to Gunn and Kinzer's (1949) laboratory data, is selected for use in this study to predict terminal raindrop fall speeds for comparison with our field observations. The selection of this parameterization was due to its simplicity and adequate accuracy level that is around ±2% with respect to Gunn and Kinzer's fall speed measurements for water drops within the diameter range of 0.5–5.0 mm:

$$V_t = \frac{(965 - 1030e^{-0.6D})}{100}. \quad (2)$$

Here, $V_t$ is raindrop terminal speed (m s$^{-1}$), and $D$ is in millimeters. The observations from artificial and natural rainfall under calm conditions found good agreement with developed

*Corresponding author*: Firat Y. Testik, firat.testik@utsa.edu

DOI: 10.1175/JHM-D-21-0004.1

models and empirical equations for raindrop characteristics such as shape, fall speed, and canting angle (Thurai and Bringi 2005; Thurai et al. 2007; Huang et al. 2008; Testik and Rahman 2016). Results from an artificial rain experiment showed good agreement between the observed raindrop shape and the model of BC1987 and between the observed fall velocity and the Gunn and Kinzer data (Thurai and Bringi 2005; Thurai et al. 2007). From the same artificial rain experiment, the mean symmetrical Gaussian canting angle distribution was near zero with a standard deviation of 7°–8° (Huang et al. 2008). Moreover, there are various field studies that reported a good agreement between raindrop fall speed observations during natural precipitation events and the laboratory data by Gunn and Kinzer (Thurai et al. 2011; Marzuki et al. 2013; Testik and Rahman 2016). However, microphysical characteristics of rainfall such as raindrop fall velocity, shape, and canting angle in the field may deviate from those observed in the laboratory (Testik et al. 2006; Montero-Martínez et al. 2009; Larsen et al. 2014; Das et al. 2020); and hence, they may deviate from the predicted values that are based on laboratory observations, due to environmental conditions such as wind (Thurai et al. 2013; Montero-Martínez and García-García 2016; Bringi et al. 2018). Deviation from the terminal speed ($V_t$) is categorized as sub- and superterminal, with subterminal referring to when raindrop fall velocity ($V_f$) is 30% slower than its terminal velocity ($V_f = 0.7V_t$) and superterminal referring to when a raindrop falls 30% faster than its terminal velocity ($V_f = 1.3V_t$) (Montero-Martínez et al. 2009). The threshold of 30% was determined according to the instrumental measurement uncertainty of Montero-Martínez et al. (2009), and we adopted the same threshold value in this study to make the comparisons between the observations from different studies possible. Raindrops with $D < 0.7$ mm were detected to have a superterminal fall speed, and the fraction of the superterminal raindrops was found to increase as diameter decreases (Montero-Martínez et al. 2009; Larsen et al. 2014). Montero Martínez et al. (2009) argued that the superterminal drops most likely occur due to small drops caused by breakups that keep falling at the same speed with the parent drop and the breakup-induced small drops increase with increasing rainfall rate. During moderate to high wind conditions, raindrops with $D > 1.0$ mm were detected to have subterminal fall speeds, and the subterminal occurrences were correlated with high wind speed and gust (Montero-Martínez and García-García 2016; Bringi et al. 2018). However, the correlation between subterminal raindrop fall velocities and wind speed was not observed by Thurai et al. (2013). Rather, it was attributed to increased drag due to raindrop oscillations, which were visualized during rainfall using high-speed imaging for the first time by Testik et al. (2006). In addition to the fall speed variations, environmental conditions might alter the shape and the canting angle of the observed raindrops from expected values. Thurai et al. (2013) observed a large percentage of raindrops to be deviating from the equilibrium shape during a convective line passage. On the other hand, compared to 7°–8° of standard deviation of the canting angle found from the artificial rain experiment, the observation from the light-to-moderate stratiform precipitation showed an increase in the standard deviation of the canting angle to 12° (Thurai and Bringi 2009).

Such deviations from the predicted values of microphysical characteristics have implications in the accuracy of our relevant estimations. For example, Pei et al. (2014) showed that raindrop fall velocity and axis ratio deviations from their predicted values can cause significant errors—reaching up to 200% errors for certain rare combinations of fall velocity and axis ratio deviations observed in field measurements—in rainfall rate retrievals using ground-based radars. Due to the low resolution and/or sensitivity issues of conventional disdrometers (Bringi et al. 2018), accurate determination of the characteristics of raindrops, especially under windy conditions, has been challenged. To fully understand raindrop behaviors under turbulent, strong-wind environments, raindrop characteristics are needed within the context of the characteristics of the surrounding atmosphere. In this article, we report our field observations of rainfall microphysical characteristics under a tornadic environment using a high-speed optical disdrometer (HOD) developed by Testik and Rahman (2016). Additionally, atmospheric conditions—such as wind speed and turbulence parameters that were captured using a 3D ultrasonic anemometer—improved the current understanding of the interaction. In section 2, the experimental method and the theoretical background are given. The results are presented in section 3, and finally, in section 4 conclusions are provided.

## 2. Methodology

Rainfall microphysical quantities were observed through in situ observations during a tornadic severe storm passage from 0010 to 0615 coordinated universal time (UTC) 25 May 2020. The National Weather Service (NWS) reported an EF1 scale tornado that had a touchdown approximately 9 km southwest of our experimental field site (NOAA 2020). The locations of the tornado touchdown (T), our field site (F), and weather radar (R) are illustrated in Fig. 1. The tornado touchdown occurred at 0111 UTC and dissipated at 0112 UTC. Composite reflectivity images from Austin/San Antonio, Texas (KEWX), weather radar are shown at the start (0100 UTC, Fig. 1a) and end (0150 UTC, Fig. 1b) of the storm passage (NOAA 2022). Figure 1c shows the field site for our observations reported in this article. The field site is located in the southwest corner of the main campus of The University of Texas at San Antonio (UTSA) with coordinates 29°34′43.4″N and 98°37′50.0″W. The field site is surrounded by short trees and vegetation with a maximum height of approximately 5 m. The average settlement height around our site is approximately 10 m with a maximum of 24 m located 460 m southeast of our site. The site is instrumented with a HOD (Testik and Rahman 2016), an R. M. Young 81000 3D ultrasonic anemometer, an OTT Parsivel$^2$ disdrometer (OTT-Hydromet 2017), an OTT Pluvio$^2$ (OTT-Hydromet 2016), and two TB4 tipping-bucket rain gauges. The estimated peak wind speed of the tornado was reported as 45 m s$^{-1}$ around the tornado touchdown location (NOAA 2020). An image of a fallen tree near our field site presented in Fig. 1d illustrates the severity

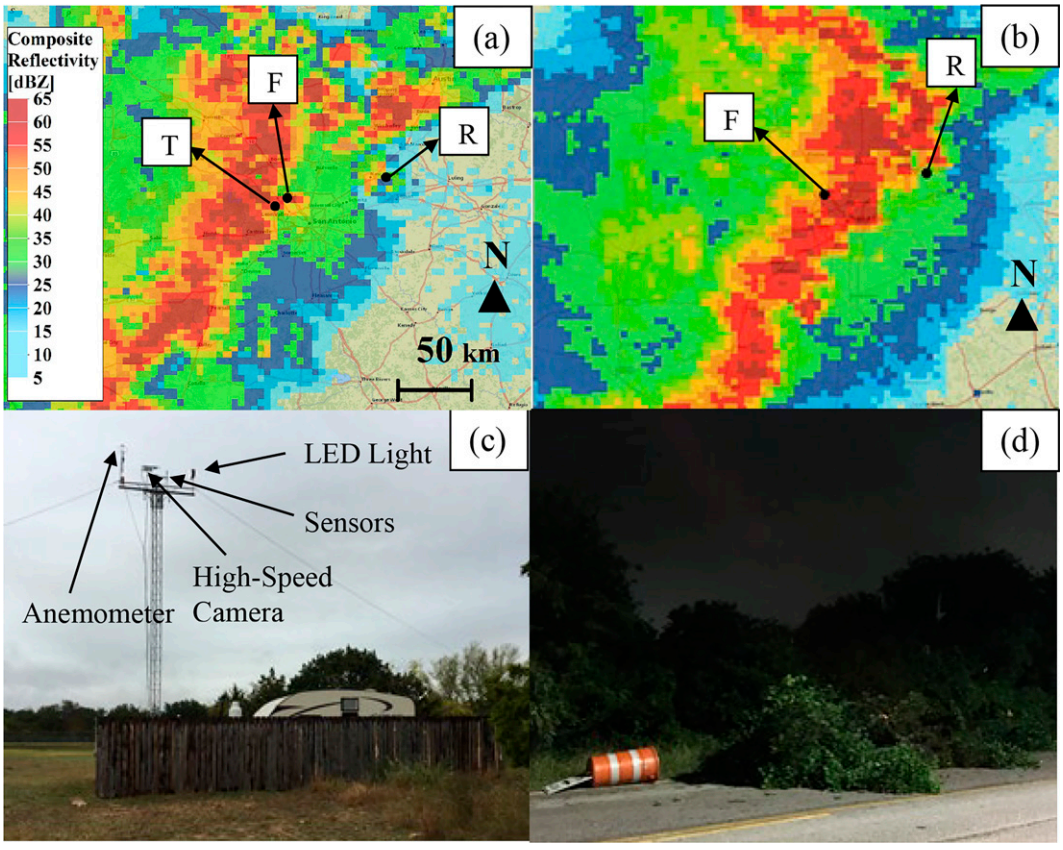


FIG. 1. Radar images show NEXRAD composite reflectivity (NCZ) from Austin/San Antonio (KEWX) weather radar during the tornadic squall-line storm at (a) 0100 UTC and (b) 0150 UTC (NOAA 2022). T, F, and R in the radar images denote the tornado touchdown, field site, and weather radar locations, respectively, and the vertical bold arrow pointing at (N) shows the north direction. (c) Photo of the field site that shows a 10-m-high tower with the HOD and sonic anemometer mounted at the top of it. (d) Fallen trees near the field site due to strong winds during the tornadic storm.

of the wind forcing during the rainfall event observed in this study. The severe storm passed through the field site from 0100 to 0150 UTC and the precipitation event continued for around four more hours with light-to-moderate wind and rainfall rates. The start and end of the storm passage were identified using both radar imagery and the wind gust speed. The lower bound of the wind speed associated with tornadic and nontornadic supercell was specified as 8 m $s^{-1}$ (Thompson 1998), to be conservative in here we defined the lower bound as 10 m $s^{-1}$ to roughly estimate the passage times. The start time of the passage was determined as 10 min before the wind gust speed first exceeded 10 m $s^{-1}$ twice or more in a subdataset that is defined later in this section, and the end time was determined as 10 min after the last time the wind gust speed exceeded 10 m $s^{-1}$.

HOD captures sequential images of raindrops that enter the measurement volume at 1000 frames per second. These images are then digitally processed to obtain raindrop characteristics such as diameter ($D$), fall speed ($V_f$), vertical to horizontal axis ratio ($\alpha$), and horizontal drift speed ($V_d$) (see Rahman and Testik 2020). Testik and Rahman (2016) describe further details of the HOD, including its firmware, software, capabilities, and measurement accuracy, which is 11% for raindrops with $D$ = 0.5 mm and decreases to 2% as the raindrop size increases to $D$ = 5.0 mm. In this study, the HOD was positioned along the northwest (320°; camera end, see Fig. 1c) to southeast (140°; light end, see Fig. 1c) direction. During strong orthogonal winds with respect to the camera view (i.e., northwest–southeast wind), raindrops that drift perpendicular to the camera view may be out of focus. While this is a major setback for the measurement accuracy of many of the optical camera systems, the measurement principle of the HOD alleviates, if not eliminates entirely, of the relevant issues. As detailed in Testik and Rahman (2016), HOD has a rectangular prism shaped measurement volume that is defined by the camera view and the width of the sensing area. Given the positioning of the HOD in this study, camera view covered an area defined by the northeast–southwest and vertical directions, and the width of the sensing area was along the northwest–southeast direction (i.e., orthogonal to the camera view). The sensing unit width is 5 mm, and the camera view is focused on an area that crosses the center of the width of the

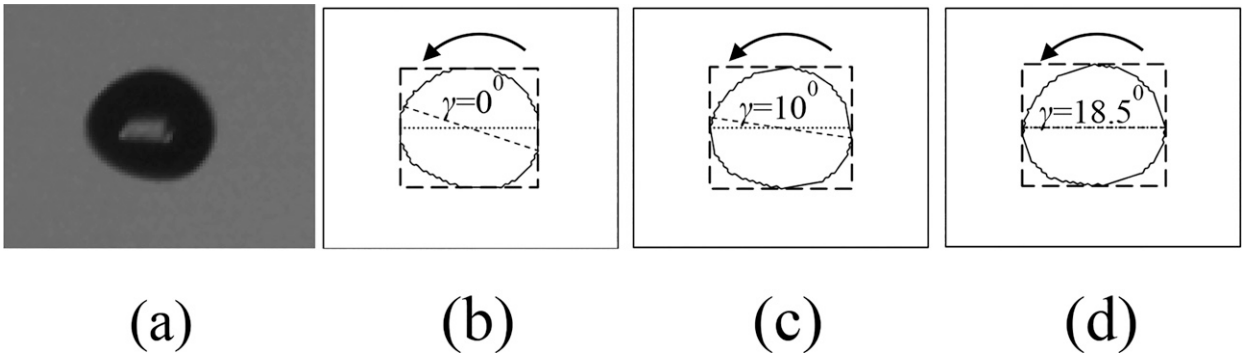


FIG. 2. Canting angle calculation steps of a raindrop with $D$ = 2.67 mm, $V_f$ = 6.74 m s$^{-1}$, $\alpha$ = 0.865, and $V_d$ = 3.59 m s$^{-1}$. (a) Raindrop raw image, (b) no rotation applied $\gamma = 0°$, here $\gamma$ denotes the rotation angle and arrow denotes the counterclockwise rotation, (c) drop boundaries are rotated $\gamma = 10°$ in counterclockwise direction, and (d) drop boundaries are rotated $\gamma = 18.5°$ in counterclockwise direction (see the text for further explanations).

sensing area. Therefore, HOD is triggered to capture raindrop images when the raindrops are within a small distance (±2.5 mm) from the camera focal plane, and HOD raindrop images are sharp. There may be cases that a raindrop may not be within the measurement volume initially, but drifted into the measurement volume and triggered the sensing unit. In such cases, the HOD software eliminates the raindrop images that are out of focus and use only the ones that are in focus to calculate the microphysical quantities for the raindrop. In addition to the capabilities described in Testik and Rahman (2016), HOD is capable of measuring raindrop canting angle within the vertical plane of the camera view frame with an uncertainty of ±3.4° for raindrops with $D > 2.0$ mm. Note that angle measurements within the vertical plane that is orthogonal to the camera view frame cannot be measured by the HOD, which is a single camera system. Therefore, while the canting angle measurements do not represent the three-dimensional geometry of the canting process, they provide valuable information for the conservative determinations of the range of canting angle values (i.e., actual canting angle value ranges are likely broader). Figure 2 illustrates the HOD canting angle calculation steps. For the HOD canting angle calculations, first, the drop edges, found by canny edge detection, were rotated from −90° to 90° at 0.5° intervals. For each rotation step, an axis-aligned minimum bounding box that encloses the raindrop edges was drawn, and the width to height ratio of the box was calculated. The canting angle was then set as the angle that gave the maximum ratio in which the drop's major axis would be parallel to the global horizontal axis. In this figure, the dotted line represents the global horizontal axis (camera frame), the long-dashed line represents the minimum bounding box surrounding the drop boundaries that is axis aligned with the camera frame, the dashed line represents the drop major axis, and the solid line represents the drop boundaries that was found from the canny edge detection algorithm. For this example case, the aspect ratio of the bounding box was found as 1.1351, 1.1381, and 1.1404 for Figs. 2b–d, respectively. The maximum aspect ratio was found as 1.1404 after rotating the drop boundaries 18.5° counterclockwise, in which the global horizontal axis and drop's major axis are aligned, indicating that the canting angle of the drop is −18.5°. Figure 3 provides examples of sequential images for oscillating, equilibrium, and canted raindrops captured by the HOD. Note that the HOD was set to capture 10 sequential images for each raindrop for these field observations, although only 6 of the images are shown in Fig. 3.

A Parsivel$^2$ disdrometer, a Pluvio$^2$ rain gauge, and two Hyquest Solutions TB4 tipping-bucket rain gauges were used to observe total rain amount (TRA) and rainfall rate ($R$) throughout the field experiment. Parsivel$^2$ is a laser optical disdrometer that can measure TRA and $R$ as well as the hydrometeors' diameters and fall speeds at 1-min resolution. Parsivel$^2$ groups diameters and fall speeds in 32 nonequidistant classes, which range from 0.062 to 25 mm and from 0.05 to 20 m s$^{-1}$, respectively (OTT-Hydromet 2017). The measurement accuracies of this instrument provided by the manufacturer are ±5% for $R$, and ±1 size class for the raindrop diameters within the range of $0.2 < D < 2.0$ mm and ±0.5 size class for raindrops with $D > 2.0$ mm. Pluvio$^2$ rain gauge is a weighing type rain gauge that has a 400 cm$^2$ catching area with a 750 mm capacity. It reports the TRA and $R$ at every minute with an accuracy of ±0.1 mm and ±6 mm h$^{-1}$, respectively (OTT-Hydromet 2016). The TB4 tipping-bucket rain gauges each have a 200-mm diameter collector and report the TRA at every minute with a 0.254-mm resolution and an accuracy of ±2% in the range of 0–250 mm h$^{-1}$ and ±3% in the range of 250–500 mm h$^{-1}$. The wind data were captured by an R. M. Young 81000 3D ultrasonic anemometer at 32 Hz. The anemometer can measure wind velocity up to 40 m s$^{-1}$ with a 0.01 m s$^{-1}$ resolution and an accuracy of ±1% for wind speeds between 0 and 30 m s$^{-1}$ and ±3% for wind speeds between 30 and 40 m s$^{-1}$. During the observations, the HOD and the anemometer were placed on top of a 10-m measurement tower, whereas the Parsivel$^2$ disdrometer, Pluvio$^2$ rain gauge, and two TB4 tipping-bucket rain gauges were mounted on top of poles with a height of 2 m. The potential interference of the presence of the sonic anemometer to raindrop measurements of HOD was minimized to the extent possible by setting a large distance (1.5 m) between the sonic anemometer and HOD measurement volume. HOD's

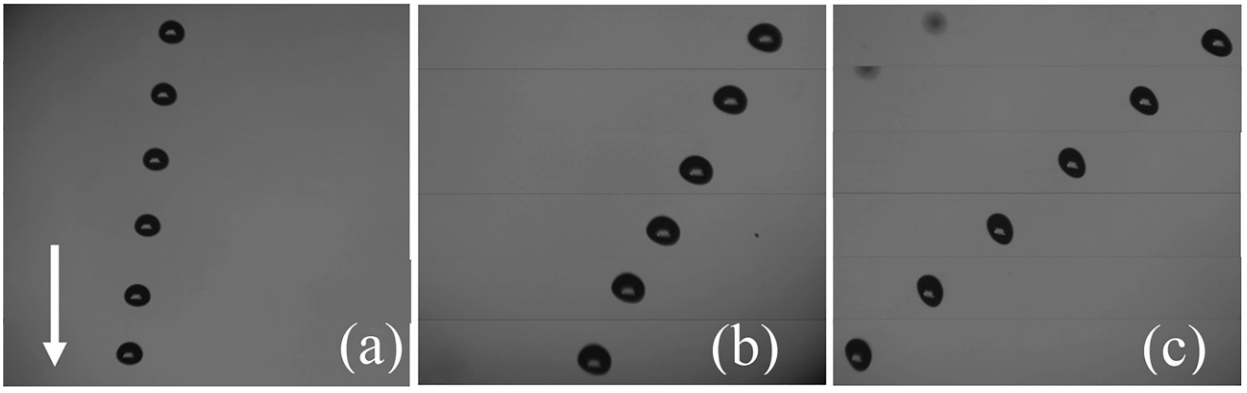


FIG. 3. Fall trajectories of (a) equilibrium-shaped ($D$ = 3.07 mm, $V_f$ = 8.04 m s$^{-1}$, $V_d$ = 0.98 m s$^{-1}$), (b) canted ($D$ = 3.83 mm, $V_f$ = 7.119 m s$^{-1}$, $V_d$ = 4.2 m s$^{-1}$, $\theta = -19.4°$), and (c) oscillating ($D$ = 3.33 mm, $V_f$ = 5.42 m s$^{-1}$, $V_d$ = 8.68 m s$^{-1}$) raindrops. Each sequence of images was obtained at a 1 m s time interval using the HOD, and for a given sequence of images, the drop images at different instances were augmented in the same frame for visualization purposes. The direction of gravity is indicated by the white arrow, and for scale, the horizontal size of each image is approximately 48.5 mm.

LED light is 80 cm from the measurement volume to minimize the flow disturbances. Similarly, the presence of physical features in and near the experimental site may introduce turbulence and flow field alterations that may have an effect on the Parsivel$^2$ measurements at 2 m; however, this effect is expected to be relatively small when considering the particle response time (especially for the large raindrops). The particle response time introduces delays in the response of raindrops to the flow field and turbulence alterations. Given the relatively large fall speeds and response times of raindrops, effects of flow disturbances on raindrop measurements by HOD and Parsivel$^2$, while still possible, are expected to be minimal.

Before wind data analysis, a spike removal procedure by Vickers and Mahrt (1997) was applied because it has been known that raindrops can cause spikes when they accumulate on the transducer face of the anemometer (Vickers and Mahrt 1997). The total number of spikes was found to be lower than 1% throughout the entire dataset, and hence, the data were used for further analysis. After the spike removal process, a double-rotation procedure was applied to align the mean wind vector to the streamwise direction and also to reduce the effect of the terrain slope on the vertical wind velocity component (Wilczak et al. 2001). Finally, the entire wind velocity dataset was divided into subdatasets of 10-min durations. Within the subdatasets, a running mean algorithm with a 240-s window was used to calculate turbulence fluctuations and other turbulence statistics of the wind velocity. The turbulent kinetic energy $k$ was calculated using Eq. (3) and the gust factor $G$ was calculated using Eq. (4):

$$k = 0.5\left(\overline{u'^2} + \overline{v'^2} + \overline{w'^2}\right), \tag{3}$$

$$G = \frac{\overline{S_3}}{\overline{S}}. \tag{4}$$

Here, $u$, $v$, and $w$ are the streamwise, lateral, and vertical wind velocity components, respectively; the prime symbol denotes the fluctuation of the respective instantaneous velocity component from the mean value, and the overbar represents time averaging. In calculating $G$, the maximum horizontal wind gust speed $\overline{S_3}$ was calculated as the maximum of the 3-s moving average of the horizontal wind speed $S$ (Suomi and Vihma 2018). The mean horizontal wind speed $\overline{S}$ was calculated from the mean of the square roots of the streamwise and lateral wind velocity components for each 10-min subdataset using the 240-s window running mean algorithm.

The turbulent kinetic energy dissipation rate $\varepsilon$ was calculated using the streamwise second-order structure function $D_u(r)$, defined in Eq. (5) (see, e.g., Davidson 2015):

$$D_u(r) = \overline{\left[u'(x + r) - u'(x)\right]^2}. \tag{5}$$

Here, $r$ is the distance between two points in space, and using Taylor's frozen hypothesis, spatial separation $r$ can be transformed into temporal separation $\tau$, and $\varepsilon$ can be calculated using one-point velocity measurements as defined in Eq. (6):

$$\varepsilon = \frac{1}{U\tau}\left[\frac{D_u(\tau)}{C_k}\right]^{1.5}. \tag{6}$$

Here, $U$ is the mean streamwise wind velocity for the subdataset, and $C_k$ is the Kolmogorov constant, equal to 2.0 in our calculations. Dissipation rate calculations for each of the 10-min-long subdatasets were conducted using a $\tau$ range of 0.1–2 s. We chose the $\tau$ range from the interval where the structure function closely follows Kolmogorov's inertial range slope $\tau^{2/3}$, as was used in previous studies (Muñoz-Esparza et al. 2018; Bodini et al. 2018, 2019).

## 3. Results and discussions

Our observations started about an hour before the tornadic storm passage, but there were not enough raindrop measurements before passage due to an insufficient amount of precipitation. For the approximately 50-min period before passage, TRA measured by Pluvio$^2$ was 0.18 mm and the average $R$

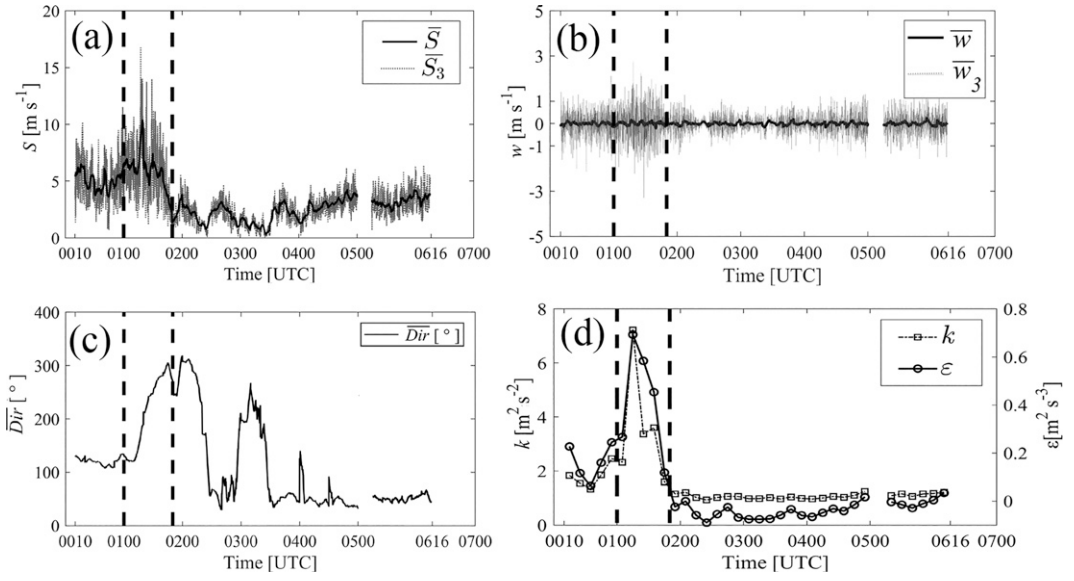


FIG. 4. Wind and turbulence characteristics for the tornadic event: (a) 240-s running mean averaged horizontal wind speed of each 10-min subdata ($\overline{S}$) and the 3-s averaged horizontal wind gust ($\overline{S_3}$); (b) 10-min averaged vertical wind velocity ($\overline{w}$) and 3-s averaged vertical wind gust ($\overline{w_3}$); (c) 240-s running mean averaged horizontal wind direction ($\overline{\mathrm{Dir}}$); and (d) turbulent kinetic energy ($k$; left ordinate) and dissipation rate ($\varepsilon$; right ordinate). The vertical dashed lines denote the start and end time of the tornado passage. The discontinuity between 0500 and 0516 UTC is due to refueling the electric generator.

was calculated as 0.22 mm $h^{-1}$ by dividing the TRA values by the corresponding time period. Therefore, the rest of the paper presents only the results that were obtained during and after the passage. Although the dataset provided here is limited to only one event, the variations of the microphysical characteristics of the raindrops between two different atmospheric turbulent conditions during and after passage and also as compared to predicted values were found to be statistically significant as shown later in this section. Sample sizes for the fall speed and axis ratio measurements in each diameter bin during and after passage were verified using statistical power and sample size calculations. The calculations indicated that the numbers of collected raindrops in all of the diameter bins are sufficient to evaluate the differences between mean and predicted [using terminal speed and axis ratio models; see Eqs. (1) and (2)] values that are larger than or equal to 10% with a power of 90%, except for the largest diameter bins during (4.25 mm) and after passage (3.75), and the smallest three diameter bins during passage (0.562, 0.687, and 0.812 mm). Since the tornadic storms are infrequent (only about 0.5 days $yr^{-1}$ in San Antonio, Brooks et al. 2003) and short lived, there are only limited raindrop microphysics data (in particular, fall speed) available in the literature (Bringi et al. 2018). Here, we provide observations on critical raindrop microphysical characteristics (including raindrop fall speed, axis ratio, canting angle, and oscillations) and turbulence during and after a tornadic storm passage and physical explanations for the observations. Data acquisition was stopped for approximately 16 min between 0500 and 0516 UTC to refill the fuel tank of the electric generator. Throughout this event, two different wind speeds and atmospheric turbulence characteristics were experienced as high (with maximum $S = 21.5$ m $s^{-1}$ and maximum $k = 7.05$ $m^2$ $s^{-2}$) and low (with maximum $S = 7.65$ m $s^{-1}$ and maximum $k = 1.19$ $m^2$ $s^{-2}$) during and after the passage, respectively. This provided favorable circumstances for comparing the effect of the wind and atmospheric turbulence on the rainfall microphysics inside the surface layer. The horizontal and vertical wind speeds, horizontal wind direction, and atmospheric turbulence characteristics of the entire event are illustrated in Figs. 4a–d, respectively, and are tabulated in Table 1. During passage, the horizontal wind speed and wind gust speed values were almost 3 times higher than those values after passage. The three second vertical wind gust $\overline{w_3}$ values were between 2.7 and −3.3 m $s^{-1}$ during passage, in which negative sign denotes the vertical wind direction toward

TABLE 1. Wind and turbulence characteristics during and after tornado passage. Here, $\overline{S}$ = averaged horizontal wind speed with 240 s running mean within 10 min of subdatasets, $\overline{S_3}$ = 3-s averaged horizontal wind gust speed, $S$ = instantaneous horizontal wind speed, $\overline{G}$ = gust factor, $k$ = turbulent kinetic energy, $\varepsilon$ = dissipation rate; $\overline{G}$, $k$, and $\varepsilon$ were calculated per each 10-min subdataset then averaged for during passage and after passage duration accordingly.

| Characteristic | During passage | After passage |
|---|---|---|
| Maximum $\overline{S}$ | 10.4 m $s^{-1}$ | 4.25 m $s^{-1}$ |
| Maximum $\overline{S_3}$ | 16.8 m $s^{-1}$ | 6.36 m $s^{-1}$ |
| Maximum $S$ | 21.5 m $s^{-1}$ | 7.65 m $s^{-1}$ |
| Average $\overline{G}$ | 2.33 | 1.87 |
| Average $k$ | 4.38 $m^2$ $s^{-2}$ | 0.56 $m^2$ $s^{-2}$ |
| Average $\varepsilon$ | 0.286 $m^2$ $s^{-3}$ | 0.02 $m^2$ $s^{-3}$ |

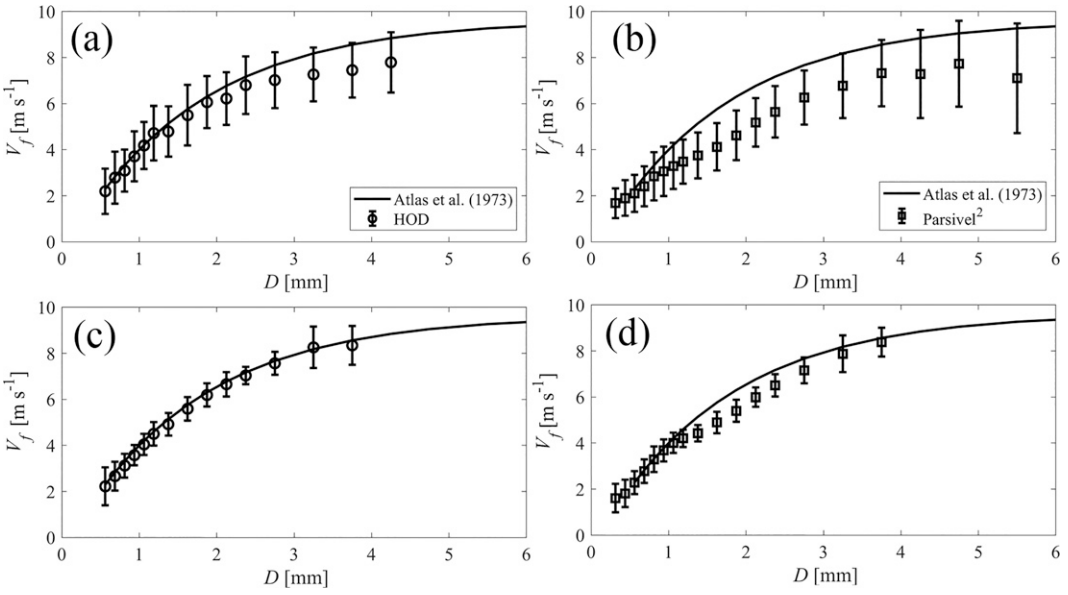


FIG. 5. Means and standard deviations (vertical bars) of the fall speeds of raindrops measured by the (a),(c) HOD (open circles) and (b),(d) Parsivel$^2$ (open squares) for each diameter bin: (a) and (b) are during the passage and (c) and (d) are after the passage. Corresponding terminal speeds predicted by Atlas et al. (1973) are shown by the solid lines.

ground, and $\overline{w_3}$ values were between 1.4 and $-1.6$ m s$^{-1}$ after passage. As can be seen in Fig. 4c, the horizontal wind direction was close to orthogonal direction to HOD's camera view frame only before passage during which there were no raindrop data and at the end of the passage for a relatively small amount of time. For the rest of the event, the horizontal wind was mainly nonorthogonal to HOD's camera view frame. The horizontal wind direction changed drastically throughout the entire experiment where 0° represents the northerly wind. During passage, the southeasterly wind gradually changed direction and eventually became northwesterly for a relatively short duration at the end of the passage. After passage the wind direction shows occasional changes but the wind was mainly from the east. The passage caused a sharp increase, by approximately one order of magnitude, on the atmospheric turbulence in terms of turbulent kinetic energy $k$ and dissipation rate $\varepsilon$. A similar increase in $\varepsilon$ was also observed by Piper and Lundquist (2004) during frontal passage in which similar wind speed characteristics occurred.

Figure 5 shows the raindrop fall speeds measured by HOD during (Fig. 5a) and after (Fig. 5c) passage and measured by Parsivel$^2$ during (Fig. 5b) and after (Fig. 5d) passage. Measured fall speed values were binned according to Parsivel$^2$ bin sizes for the volume equivalent diameter (OTT-Hydromet 2017). In this figure, measured fall speeds were compared with the predicted terminal fall speed values ($V_t$) using the relationship given in Eq. (2). Identification of the sub- and superterminal raindrops was conducted by comparing HOD measured fall speed of each raindrop with the predicted terminal speed from Eq. (2) and by using the criterion of 30% speed deviation from the predicted value as the threshold for sub- and superterminal raindrops as specified by Montero-Martínez et al. (2009) based on their measurement uncertainties. As can be seen in this figure, the observed fall speeds by both Parsivel$^2$ and HOD indicate dominance of subterminal raindrops during passage. The subterminality and standard deviations of fall speeds during passage were higher for Parsivel$^2$ measurements than HOD measurements. The onset of the subterminality for Parsivel$^2$ measurements was around $D > 0.7$ mm whereas the onset was around $D > 1.5$ mm for HOD measurements. Note that HOD measurements were used for the rest of the quantitative and statistical analyses in this study. Two separate one-sample $t$ tests with 0.05 significance level were performed to test whether or not the fall speed means ($\mu^D_{V_f}$ for during passage, $\mu^A_{V_f}$ for after passage) for each diameter bin deviate from the predicted terminal fall speed ($V_t$) for the corresponding bin. Also, a two-sample $t$ test with 0.05 significance level was performed to test the statistical significance of the differences between fall speed means during and after passage. In these tests, the null hypotheses for one-sample $t$ tests were $\mu^D_{V_f} = V_t$ and $\mu^A_{V_f} = V_t$ for during and after passage, respectively. The null hypothesis for the two-sample $t$ test was $\mu^D_{V_f} = \mu^A_{V_f}$. The results of these statistical tests are tabulated in Table 2. The $t$-test results showed that, during passage, the differences between raindrop fall speeds and the corresponding predicted terminal speeds were statistically significant for diameter bins with $D \geq 1.375$ mm, except for the diameter bin of 4.25 mm. For the 4.25-mm diameter bin, the $t$ test failed to reject the null hypothesis as the sample size was insufficient for this bin. Effect size tests showed that Cohen's $d$ values were ranging between 0.54 and 0.94 for diameter bins 2.75 mm and larger, indicating medium to large effect sizes for these raindrops during passage. After passage, while the differences between fall speeds and predicted

TABLE 2. Sample means ($\hat{\mu}_{V_f}^{D}$, during passage; $\hat{\mu}_{V_f}^{A}$, after passage) and standard deviations ($\hat{\sigma}_{V_f}^{D}$, during passage; $\hat{\sigma}_{V_f}^{A}$, after passage) estimated from HOD raindrop fall speed measurements; $p$ values of one-sample $t$ tests corresponding to samples during and after passage are shown as $p_t^{D,V}$ and $p_t^{A,V}$, respectively; and $p$ value of the two-sample $t$ test is shown as $p_f^{D-A,V}$.

| | | During passage | | | | After passage | | | | |
|---|---|---|---|---|---|---|---|---|---|---|
| $D$[a] (mm) | $V_t$ (m s$^{-1}$) | $\hat{\mu}_{V_f}^{D}$ (m s$^{-1}$) | $\hat{\sigma}_{V_f}^{D}$ (m s$^{-1}$) | $N$[b] (—) | $p_t^{D,V}$ (—) | $\hat{\mu}_{V_f}^{A}$ (m s$^{-1}$) | $\hat{\sigma}_{V_f}^{A}$ (s$^{-1}$) | $N$ (—) | $p_t^{A,V}$ (—) | $p_f^{D-A,V}$ (—) |
| 0.562 | 2.298 | 2.193 | 0.979 | 82 | 0.335 | 2.222 | 0.821 | 94 | 0.370 | 0.836 |
| 0.687 | 2.829 | 2.787 | 1.129 | 65 | 0.763 | 2.666 | 0.623 | 137 | 0.003 | 0.42 |
| 0.812 | 3.322 | 3.090 | 0.913 | 80 | 0.026 | 3.123 | 0.517 | 196 | 0.000 | 0.766 |
| 0.937 | 3.779 | 3.709 | 1.089 | 83 | 0.555 | 3.576 | 0.444 | 248 | 0.000 | 0.281 |
| 1.062 | 4.203 | 4.183 | 1.021 | 68 | 0.867 | 4.042 | 0.455 | 234 | 0.000 | 0.273 |
| 1.187 | 4.597 | 4.719 | 1.190 | 77 | 0.371 | 4.502 | 0.507 | 248 | 0.004 | 0.123 |
| 1.375 | 5.136 | 4.789 | 1.092 | 135 | 0.000 | 4.922 | 0.494 | 476 | 0.000 | 0.176 |
| 1.625 | 5.765 | 5.497 | 1.312 | 118 | 0.029 | 5.593 | 0.510 | 312 | 0.000 | 0.446 |
| 1.875 | 6.306 | 6.062 | 1.131 | 109 | 0.026 | 6.189 | 0.503 | 209 | 0.000 | 0.266 |
| 2.125 | 6.772 | 6.221 | 1.139 | 81 | 0.000 | 6.659 | 0.530 | 156 | 0.009 | 0.001 |
| 2.375 | 7.173 | 6.805 | 1.251 | 63 | 0.023 | 7.036 | 0.374 | 75 | 0.002 | 0.162 |
| 2.75 | 7.672 | 7.021 | 1.216 | 103 | 0.000 | 7.567 | 0.496 | 67 | 0.087 | 0.000 |
| 3.25 | 8.185 | 7.266 | 1.171 | 58 | 0.000 | 8.259 | 0.903 | 22 | 0.699 | 0.000 |
| 3.75 | 8.564 | 7.455 | 1.185 | 20 | 0.000 | 8.347 | 0.842 | 5 | 0.595 | 0.118 |
| 4.25 | 8.846 | 7.794 | 1.307 | 3 | 0.298 | | | | | |

[a] Mid size of the diameter bin in millimeters.
[b] Raindrop count for the diameter bin.

terminal speeds of raindrops were also statistically significant for most of the diameter bins, the differences were relatively small with Cohen's $d < 0.5$ for all $D$ bins. The two-sample $t$ test results indicated differences in raindrop fall speed means during and after passage were statistically significant only for the diameter bins of 2.125, 2.75, and 3.25 mm. The test failed to reject the null hypothesis for most of the diameter bins. We also conducted an $F$ test with 0.05 significance level for equality of variances of raindrop fall speeds during and after passage. The results of the $F$ test indicated that the variances of the fall speeds during and after passage were unequal, except for diameter bins of 0.562, 3.25, and 3.75 mm. This finding provides sufficient evidence to state that raindrops' fall speed variance changes under strong wind and turbulence conditions.

During passage, 9.4% of the raindrops with $D > 1.0$ mm were observed to have subterminal fall speeds. Montero-Martínez and García-García (2016) found a subterminal raindrop percentage as high as 20% under moderate wind speeds. The difference may be due to a number of factors, such as the uncertainty level (30%–40%) of the instrument used by Montero-Martínez and García-García (2016) and that of the HOD used in our study (maximum 11% for raindrops with $D = 0.5$ mm and decreases with increasing diameter), binwise categorization of the raindrop fall speeds, and different wind speed and turbulence levels. After passage, only 0.5% of the drops $D > 1.0$ mm were found to have subterminal fall speeds, and the observed fall speeds agreed well with the Atlas et al. (1973) prediction with decreasing wind speed and turbulence levels as reported by Montero-Martínez and García-García (2016) and Bringi et al. (2018). On the other hand, approximately 26% of the drops with a diameter between $0.5 < D < 1.0$ mm were identified as subterminal, and approximately 14.5% of drops of the same size were detected as superterminal during passage. After passage, 6.5% and 3.5% of the raindrops with $D < 1.0$ mm were observed to have sub- and superterminal fall speeds, respectively. Montero-Martínez et al. (2009) reported that 20% of the drops for the bin size of $D \approx 0.64$ mm as superterminal during heavy rainfall period of their study. However, the subterminal percentage of drops regardless of the size was given as less than 5%. The percentage of raindrops with a superterminal fall speed was reported as increasing with decreasing drop diameter up to about 80% ($D \approx 0.24$ mm) by Montero-Martínez et al. (2009). The reason for the high presence of superterminal raindrops was claimed to be because the large drops fragment, and the fragments continue falling at the same speed of parent drop, where incidents of fragmentation increase with increasing $R$ (Montero-Martínez et al. 2009). Using two-dimensional video disdrometer (2DVD), Larsen et al. (2014) concluded that instrument-induced splash can only produce a negligible amount of superterminal drops, supporting that superterminal drops exist in natural precipitation events. However, the $R$ and wind conditions of the events were not provided with the observed percentages of raindrops with subterminal fall speeds in Larsen et al. (2014). Bringi et al. (2018) highlighted that it is not clear whether or not the well-known erroneous fall speed estimation of the 2DVD for the mismatched small raindrops ($D < 0.5$ mm) was accounted for by Larsen et al. (2014). It is evident that in natural rainfall events, raindrops with superterminal fall speeds exist, which is also supported by the HOD measurements. However, our data do not show a distinct superterminal behavior for small drops in the range of $0.5 < D < 1.0$ mm as reported by Montero-Martínez et al. (2009) and Larsen et al. (2014). In addition to wind shear and turbulence, collision-induced fragmentation prior to the sampling by the HOD might be another plausible cause for the presence of superterminal raindrops. However, as the raindrop collision occurrence frequencies reported by Testik and Rahman (2017) based on the raindrop collision observations

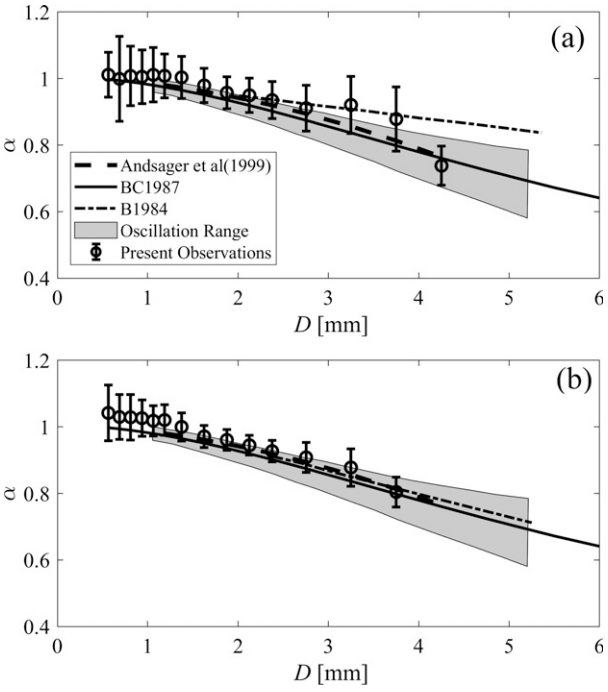


FIG. 6. Means (open circles) and standard deviations (vertical bars) of the axis ratios of the raindrops measured by the HOD for each diameter bin: (a) during the passage, and (b) after the passage. Axis ratio values predicted by Eq. (3) of Andsager et al. (1999), by the polynomial fit to the BC1987 model, and by the B1984 model [for average rainfall rate (a) $R = 50$ mm h$^{-1}$ and (b) $R = 5$ mm h$^{-1}$], as well as the drop oscillation range by Thurai and Bringi (2009) are provided for comparison.

in the field for the first time using the HOD, raindrop collision process is likely not a primary cause for the presence of superterminal drops. After passage, the fall speeds measured by HOD generally agreed well with the predictions of the parameterization by Atlas et al. (1973) whereas Parsivel$^2$ measurements deviated from terminal fall speeds for raindrops with $1 < D < 3$ mm. However, these deviations of the Parsivel$^2$ measurements (see Figs. 5b,d) and the standard deviations of fall speed measurements by both of the instruments after passage were smaller than those during passage.

Axis ratios of the raindrops ($\alpha$) observed by the HOD during this event are given in Fig. 6. In this figure, the observed axis ratios are compared with the predictions of BC1987 using the polynomial fit in Eq. (1). A shaded region enveloping BC1987's predictions is incorporated into the figure to demonstrate potential deviation from the predicted values, according to the drop oscillations observed in a wind tunnel study by Thurai and Bringi (2009). In this figure, Andsager et al.'s (1999) empirical representation of the mean $\alpha$ distribution for oscillating raindrops in a still-air laboratory fall column [Eq. (3) in Andsager et al. 1999] and Beard's (1984, hereafter B1984) axis ratio predictions for different $R$ values are also presented. B1984 model considers collisional forcing and utilizes $R$ values to obtain oscillation probabilities and predict $\alpha$ distributions. In the tornadic event studied, two different average $R$ values were calculated for during and after passage. The average $R$ values were calculated by dividing the TRA values by the corresponding time durations of the during and after tornado passage intervals. Since Parsivel$^2$ underestimates the TRA and $R$ during strong winds and high turbulence, only Pluvio$^2$ and the TB4 rain gauges were used to calculate the average $R$ (Angulo-Martínez and Barros 2015). It should be noted that while rain gauges, including Pluvio$^2$ and TB4 rain gauges, are subject to potential rainfall undercatch during windy conditions, they have been widely used to measure TRA and $R$ even during such conditions (Pollock et al. 2018). The average $R$ values from Pluvio$^2$ measurements were 49.96 and 3.66 mm h$^{-1}$ during and after passage, respectively, and the average $R$ values from the average recordings of the two TB4 rain gauges were 51.99 and 3.81 mm h$^{-1}$ during and after passage, respectively. The sampling durations of the specified during and after passage periods were 50 and 255 mins, respectively. Therefore, to compare our observations with predicted values, $R$ values in the B1984 model were set to 50 and 5 mm h$^{-1}$ for comparisons during and after passage, respectively. Two separate one-sample $t$ tests with 0.05 significance level were also performed for the raindrop axis ratios during and after passage to test whether or not the axis ratio means ($\mu_\alpha^D$ for during passage, $\mu_\alpha^A$ for after passage) for each diameter bin deviate from the predicted axis ratio ($\mathrm{BC}_\alpha$) values for the corresponding bin by the BC1987 model. In addition, a two-sample $t$ test with 0.05 significance level was performed to test the statistical significance of the differences between axis ratio means during and after passage. In these tests, the null hypotheses for one-sample $t$ tests were $\mu_\alpha^D = \mathrm{BC}_\alpha$ and $\mu_\alpha^A = \mathrm{BC}_\alpha$ during and after passage, respectively. The null hypothesis for the two-sample $t$ test was $\mu_\alpha^D = \mu_\alpha^A$. The results of the $t$ tests are tabulated in Table 3. Note that, since the axis ratios of raindrops with $D < 1.0$ mm are close to 1 without showing a notable change with changes in raindrop size and there are larger measurement uncertainties for these smaller raindrops, we considered the axis ratio of raindrops with $D > 1$ mm in our analysis. For the one-sample $t$ tests, the null hypotheses were rejected for all of the diameter bins ($D > 1$ mm), except for the largest bins during ($D > 4.0$ mm) and after passage ($D > 3.5$ mm). This result indicates that raindrop axis ratios show statistically significant differences from BC1987 model predictions for both during and after passage. The two-sample $t$ test results indicate that the differences between the raindrop axis ratios during and after passage were statistically significant for diameter bins larger than 3.0 mm. For the rest of the diameter bins ($3.0 > D > 1.0$ mm), the test failed to reject the null hypothesis. A likely reason for failing to reject the null hypothesis is that surface tension force for this raindrop size range may be sufficient in overcoming the shape alteration effects of the high wind and turbulence conditions for the event considered. The $\alpha$ distribution of larger drops ($D > 2.0$ mm) during passage (Fig. 6a) deviates significantly from the BC1987 model and the probable cause of these deviations is the strong wind- and turbulence-induced raindrop morphological changes, including raindrop oscillations and those changes associated with the changes in the aerodynamic and hydrodynamic force balance

TABLE 3. Sample means ($\hat{\mu}_\alpha^D$, during passage; $\hat{\mu}_\alpha^A$, after passage) and standard deviations ($\hat{\sigma}_\alpha^D$, during passage; $\hat{\sigma}_\alpha^A$, after passage) estimated from HOD raindrop axis ratio measurements; $p$ values of one-sample $t$ tests corresponding to samples during and after passage are shown as $p^{D-\mathrm{BC}\alpha}$ and $p^{A-\mathrm{BC}\alpha}$, respectively; and $p$ value of the two-sample $t$ test is shown as $p^{D-A,\alpha}$.

| | | During passage | | | | After passage | | | | |
|---|---|---|---|---|---|---|---|---|---|---|
| $D$[a] | $\mathrm{BC}_\alpha$[b] | $\hat{\mu}_\alpha^D$ | $\hat{\sigma}_\alpha^D$ | $N$[c] | $p^{D-\mathrm{BC}\alpha}$ | $\hat{\mu}_\alpha^A$ | $\hat{\sigma}_\alpha^A$ | $N$ | $p^{A-\mathrm{BC}\alpha}$ | $p^{D-A,\alpha}$ |
| 0.562 | 0.998 | 1.011 | 0.067 | 82 | 0.066 | 1.042 | 0.084 | 94 | 0.000 | 0.008 |
| 0.687 | 0.994 | 0.999 | 0.128 | 65 | 0.739 | 1.029 | 0.068 | 137 | 0.000 | 0.073 |
| 0.812 | 0.989 | 1.008 | 0.089 | 80 | 0.078 | 1.029 | 0.069 | 196 | 0.000 | 0.06 |
| 0.937 | 0.985 | 1.005 | 0.081 | 83 | 0.024 | 1.026 | 0.055 | 248 | 0.000 | 0.03 |
| 1.062 | 0.980 | 1.011 | 0.082 | 68 | 0.002 | 1.018 | 0.046 | 234 | 0.000 | 0.494 |
| 1.187 | 0.974 | 1.008 | 0.066 | 77 | 0.000 | 1.021 | 0.046 | 248 | 0.000 | 0.125 |
| 1.375 | 0.965 | 1.004 | 0.063 | 135 | 0.000 | 0.999 | 0.042 | 476 | 0.000 | 0.535 |
| 1.625 | 0.951 | 0.979 | 0.052 | 118 | 0.000 | 0.971 | 0.033 | 312 | 0.000 | 0.128 |
| 1.875 | 0.936 | 0.957 | 0.048 | 109 | 0.000 | 0.961 | 0.031 | 209 | 0.000 | 0.504 |
| 2.125 | 0.919 | 0.949 | 0.052 | 81 | 0.000 | 0.945 | 0.029 | 156 | 0.000 | 0.431 |
| 2.375 | 0.902 | 0.935 | 0.056 | 63 | 0.000 | 0.927 | 0.032 | 75 | 0.000 | 0.419 |
| 2.75 | 0.875 | 0.911 | 0.069 | 103 | 0.000 | 0.908 | 0.045 | 67 | 0.000 | 0.773 |
| 3.25 | 0.837 | 0.921 | 0.086 | 58 | 0.000 | 0.878 | 0.056 | 22 | 0.002 | 0.012 |
| 3.75 | 0.798 | 0.878 | 0.096 | 20 | 0.001 | 0.804 | 0.045 | 5 | 0.782 | 0.025 |
| 4.25 | 0.761 | 0.738 | 0.059 | 3 | 0.576 | | | | | |

[a] Mid size of the diameter bin in millimeters.
[b] Axis ratio values of BC1987 model.
[c] Raindrop count for the diameter bin.

that determines the steady-state raindrop shape (Beard 1984; Tokay and Beard 1996; Testik and Barros 2007). Raindrop oscillations can be attributed to various factors, including collision, vortex shedding, turbulence, and shear (Beard 1984; Tokay and Beard 1996; Testik and Barros 2007). During passage, the B1984 model generally agreed well with the observed $\alpha$ distribution for $D > 2.0$ mm except for the largest bin size ($D = 4.25$ mm), which agreed with the BC1987 model—also observed by Chandrasekar et al. (1988) for $D > 4.0$ mm. Chandrasekar et al. (1988) noted that a possible cause of observed oscillation suppression in the largest drops may be the continued presence of the unmelted ice cores inside such large drops. Nevertheless, we have insufficient raindrop observations for $D > 4.0$ mm to make definitive conclusions. Agreement of the observed raindrops (for the approximate diameter range of $2.0 < D < 4.0$ mm) with the B1984 model during passage may be considered as an indication of the oscillation of large drops that occurs almost only through collision. While the calculated collision rate predictions for still air conditions were found to be too low to cause these large observed deviations (see, e.g., Tokay and Beard 1996; Testik and Rahman 2017), such a conclusion cannot be drawn for the tornadic conditions considered in this study as strong wind and turbulence likely increase the collision rates and as there is no available model to reliably predict the collision rates during the tornadic conditions. Nevertheless, according to Andsager et al. (1999), the B1984 model overestimates the oscillation amplitudes caused by collision due to underestimations of the viscous dissipation estimations. This suggests that agreement of our raindrop axis ratio observations with the B1984 model predictions during passage may be coincidental. Since a difference was also found between present observations and the distribution of vortex shedding induced oscillations provided by Andsager et al. (1999), other forcing mechanisms might be affecting the $\alpha$ deviations during passage, such as turbulence and wind shear. The shear flow was found to cause variations in drag and lift coefficients for spherical water droplets, and an increment in the $\alpha$ of almost 14% (Sugioka and Komori 2007; Suh and Lee 2013). Strong shear flow and turbulence, which continuously alter the drag and lift coefficients of raindrops and increases their oscillation amplitudes, may be the possible major sources of $\alpha$ deviation. After the passage under low-to-moderate wind and turbulence conditions, the $\alpha$ distribution for larger drops ($D > 2.0$) was slightly underestimated by the B1984 model and the distribution provided by Andsager et al. (1999). The $\alpha$ values of midsized ($1.0 < D < 2.0$ mm) raindrops did not show any distinct difference during and after passage. However, the standard deviations of $\alpha$ for the midsized raindrops during passage were higher than those after passage for all of the $D$ bins, except for the smallest $D$ bin of 0.562 mm.

The percentages of oscillating raindrops within a given raindrop bin size were given in Table 4 during and after passage to emphasize the effect of high wind and shear during passage on the raindrop shape. The numbers of oscillating raindrops were determined by visual inspection of the HOD images for the entire event. Visual inspections encompassed totals of 835 and 1804 raindrops during and after passage, respectively. Raindrops were specified as oscillating raindrops, if continuous shape alterations were clearly present in the sequential HOD images, which were captured as the raindrops fall within the HOD's measurement volume. An example of an oscillating raindrop observation by the HOD is provided in Fig. 3c. The reported numbers for oscillating raindrops are conservative values, underestimating actual raindrop oscillation occurrences, as we omitted raindrops with less than 4 clear sequential images and with $D < 1.0$ mm when

TABLE 4. Total number of captured raindrops by HOD and percentage of oscillating raindrops for each diameter bin. For the entire diameter bin range (0.499–4.499 mm), 5.8% of the total number of raindrops (i.e., 1145 raindrops) and 0.5% of the total number of raindrops (i.e., 2479 raindrops) were oscillating during passage and after passage, respectively.

| | During passage | | After passage | |
|---|---|---|---|---|
| $D$[a] | $N$[b] | Oscillating drops (%) | $N$ | Oscillating drops (%) |
| 0.562 | 82 | — | 94 | — |
| 0.687 | 65 | — | 137 | — |
| 0.812 | 80 | — | 196 | — |
| 0.937 | 83 | — | 248 | — |
| 1.062 | 68 | — | 234 | — |
| 1.187 | 77 | 1.29 | 248 | — |
| 1.375 | 135 | 1.48 | 476 | 0.84 |
| 1.625 | 118 | 5.93 | 312 | 0.31 |
| 1.875 | 109 | 5.50 | 209 | 0.96 |
| 2.125 | 81 | 9.88 | 156 | 1.93 |
| 2.375 | 63 | 19.05 | 75 | 1.35 |
| 2.75 | 103 | 16.50 | 67 | 1.5 |
| 3.25 | 58 | 10.34 | 22 | 4.77 |
| 3.75 | 20 | 25.00 | 5 | — |
| 4.25 | 3 | 33.33 | | |

[a] Mid size of the diameter bin in millimeters.
[b] Raindrop count for the diameter bin.

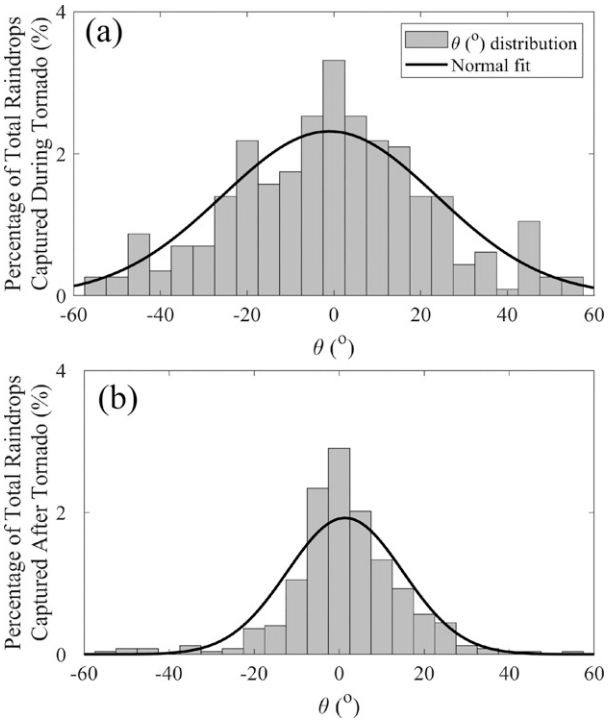


FIG. 7. Percentage of total raindrops measured by the HOD in each raindrop canting angle, $\theta$, bin: (a) during and (b) after the passage. Note that canting angle calculations were performed only for raindrops with $D > 2.0$ mm due to measurement uncertainty considerations. Canting angle bins are 5° wide and centered around $\theta = 0°$. Mean $\theta$ values were found as $-1.0°$ with a standard deviation of 24.7° and average of 1.4° with a standard deviation of 13.6° during and after passage, respectively.

determining oscillation occurrences. Moreover, low-amplitude oscillations that were too difficult to identify through visual inspection are not included in the reported total numbers of oscillating raindrops. Table 4 indicates that approximately 5.8% and 0.5% of the raindrops were oscillating during and after the passage, respectively. The breakdown of the oscillating raindrop percentages for each diameter bin during passage shows that oscillating raindrop percentage has an increasing trend with increasing raindrop size. This may be partially explained by the increasing effects of surface tension forces in resisting drop oscillations as the drop size decreases and also by the difficulties in visual identification of oscillating raindrops for smaller sizes. A two-sample $t$ test with 0.05 significance level was performed to test the statistical significance of the differences between raindrop oscillation percentages during and after passage. The result of this test showed that the difference was statistically significant and that there is sufficient evidence to state that there were larger percentages of oscillating raindrops during passage than after passage. Under calm wind conditions, Testik et al. (2006) showed that oscillating raindrops have subterminal fall speeds and also have horizontal drift speeds ($V_d$) of 20%–30% of their terminal speeds. In the present study, oscillating raindrops with horizontal drift speeds even higher than their corresponding terminal speeds were observed due to strong wind. An example of such an oscillating raindrop is provided in Fig. 3c. This example raindrop had a subterminal fall speed of 5.42 m $s^{-1}$ (=0.657$V_t$) and a horizontal drift speed of 8.68 m $s^{-1}$ (=1.05 $V_t$).

The distribution of canting angles during and after passage is shown in Fig. 7. During the passage, the mean canting angle ($\theta$) was $-1.0°$ with a standard deviation ($\sigma_\theta$) of 24.7°. After the passage, $\theta$ was 1.4° with a $\sigma_\theta$ of 13.6°. The canting angle calculation was done only for the drops with $D > 2.0$ mm because the calculation of the canting angle of drops with $D < 2$ mm introduces additional uncertainties due to available pixel resolutions. Observed $\sigma_\theta$ and percentages of occurrence after the passage in this study are in good agreement with those reported by Thurai and Bringi (2009). In their observation of light-to-moderate stratiform precipitation, $\theta$ was reported to have a mean value of 0° with $\sigma_\theta$ as 12°, and only 3% of the raindrops were found to have $\theta$ larger than 15° (Thurai and Bringi 2009). In our study, approximately 13.6% and 2.5% of the total raindrops were found to have canting angles larger than 15° during and after passage, respectively. Our observations show that $\theta$ remains close to zero while the $\sigma_\theta$ increases in a windy turbulent environment. The distribution of the canting angle was found to be fairly symmetrical around mean values with a skewness of 0.006, and $-0.35$ during and after the passage, respectively.

## 4. Conclusions

This study presents observations on the rainfall microphysical characteristics during a tornadic severe storm. An increment of approximately one order of magnitude was observed

in atmospheric turbulence in terms of $k$ and $\varepsilon$ during the tornado passage compared to after the passage. Moreover, the horizontal wind speed and wind gust speed were 3 times higher during the passage than after the passage. This created favorable conditions for investigating the effects of wind shear and turbulence on raindrop microphysics.

We found that 9.4% of the raindrops with $D > 1.0$ have subterminal fall velocities under the strong wind shear and highly turbulent environment. However, we could not find any distinct superterminal fall velocity behavior for the raindrops within the size range of $0.5 < D < 1.0$ mm for the observed rainfall event, which was previously reported by Montero-Martínez et al. (2009) and Larsen et al. (2014). The differences in the smallest measured raindrop sizes and in the experienced wind shear and turbulence levels might be couple of the causes of this discrepancy.

Substantial raindrop axis ratio deviations from BC1987 were observed during and after passage. During passage, good agreement was found between the observed axis ratio and the B1984 model for raindrops with $2.0 < D < 4.0$ mm whereas after passage, the B1984 model did not agree well with the observed axis ratio distribution for the same size range. Andsager et al. (1999, coauthored also by the author of B1984 model) notes that the viscous dissipation considerations in the model of B1984 lead to overestimations of the collision-induced oscillation amplitudes. Therefore, we could not conclude an actual agreement between our axis ratio observations and predictions by B1984 model based on raindrop collision process solely. Wind shear- and turbulence-induced raindrop shape deformations (discussed in this article in terms of raindrop oscillations and canting) are important in the observed axis ratio deviations. The axis ratio distributions of midsized ($1.0 < D < 2.0$ mm) raindrops did not show any distinct difference between the time periods of during and after passage. Though the mean axis ratio of these drops was found to be approximately similar during and after passage, the standard deviations were slightly higher during passage for the midsized raindrops ($1.0 < D < 2.0$ mm). Finally, our observations show that the changes in the mean canting angle $\theta$ values during and after passage were within the HOD's measurement uncertainty level, indicating that wind and turbulence had limited effect on $\theta$ values for this event. However, the standard deviation values for the canting angle $\sigma_\theta$ were about 80% larger during passage than after passage, which clearly demonstrated the effect of wind and turbulence on the canting angle variations.

Rainfall microphysical quantities are critical in rainfall amount and rate measurements and estimations by, for example, ground-based disdrometers and dual-polarization weather radars. It is vital to provide accurate raindrop characteristics since the estimation accuracy of $R$ and TRA values plays an important role in a vast array of other applications. Field observations during a tornadic storm reported in this study provide valuable information on raindrop characteristics under strong wind and turbulence for improved $R$ and TRA measurements and estimations in such environments.

*Acknowledgments.* This research was supported by the funds provided by the National Science Foundation under Grant AGS-1741250 to the second author (FYT). The first author is a graduate student under the guidance of FYT. The authors are grateful to Prof. Dr. Murat C. Testik for his valuable comments and discussions on the statistical analyses of the dataset.

## REFERENCES

Andsager, K., K. V. Beard, and N. F. Laird, 1999: Laboratory measurements of axis ratios for large raindrops. *J. Atmos. Sci.*, **56**, 2673–2683, https://doi.org/10.1175/1520-0469(1999)056<2673:LMOARF>2.0.CO;2.

Angulo-Martínez, M., and A. P. Barros, 2015: Measurement uncertainty in rainfall kinetic energy and intensity relationships for soil erosion studies: An evaluation using PARSIVEL disdrometers in the Southern Appalachian Mountains. *Geomorphology*, **228**, 28–40, https://doi.org/10.1016/j.geomorph.2014.07.036.

Atlas, D., R. C. Srivastava, and R. S. Sekhon, 1973: Doppler radar characteristics of precipitation at vertical incidence. *Rev. Geophys.*, **11**, 1–35, https://doi.org/10.1029/RG011i001p00001.

Beard, K. V., 1976: Terminal velocity and shape of cloud and precipitation drops aloft. *J. Atmos. Sci.*, **33**, 851–864, https://doi.org/10.1175/1520-0469(1976)033<0851:TVASOC>2.0.CO;2.

——, 1977: Terminal velocity adjustment for cloud and precipitation drops aloft. *J. Atmos. Sci.*, **34**, 1293–1298, https://doi.org/10.1175/1520-0469(1977)034<1293:TVAFCA>2.0.CO;2.

——, 1984: Oscillation models for predicting raindrop axis and backscatter ratios. *Radio Sci.*, **19**, 67–74, https://doi.org/10.1029/RS019i001p00067.

——, and H. R. Pruppacher, 1969: A determination of the terminal velocity and drag of small water drops by means of a wind tunnel. *J. Atmos. Sci.*, **26**, 1066–1072, https://doi.org/10.1175/1520-0469(1969)026<1066:ADOTTV>2.0.CO;2.

——, and C. Chuang, 1987: A new model for the equilibrium shape of raindrops. *J. Atmos. Sci.*, **44**, 1509–1524, https://doi.org/10.1175/1520-0469(1987)044<1509:ANMFTE>2.0.CO;2.

——, and R. J. Kubesh, 1991: Laboratory measurements of small raindrop distortion. Part 2: Oscillation frequencies and modes. *J. Atmos. Sci.*, **48**, 2245–2264, https://doi.org/10.1175/1520-0469(1991)048<2245:LMOSRD>2.0.CO;2.

——, ——, and H. T. Ochs, 1991: Laboratory measurements of small raindrop distortion. Part I: Axis ratios and fall behavior. *J. Atmos. Sci.*, **48**, 698–710, https://doi.org/10.1175/1520-0469(1991)048<0698:LMOSRD>2.0.CO;2.

Best, A. C., 1950: Empirical formulae for the terminal velocity of water drops falling through the atmosphere. *Quart. J. Roy. Meteor. Soc.*, **76**, 302–311, https://doi.org/10.1002/qj.49707632905.

Bodini, N., J. K. Lundquist, and R. K. Newsom, 2018: Estimation of turbulence dissipation rate and its variability from sonic anemometer and wind Doppler lidar during the XPIA field campaign. *Atmos. Meas. Tech.*, **11**, 4291–4308, https://doi.org/10.5194/amt-11-4291-2018.

——, ——, R. Krishnamurthy, M. Pekour, L. K. Berg, and A. Choukulkar, 2019: Spatial and temporal variability of turbulence dissipation rate in complex terrain. *Atmos. Chem. Phys.*, **19**, 4367–4382, https://doi.org/10.5194/acp-19-4367-2019.

Bringi, V., M. Thurai, and D. Baumgardner, 2018: Raindrop fall velocities from an optical array probe and 2-D video disdrometer. *Atmos. Meas. Tech.*, **11**, 1377–1384, https://doi.org/10.5194/amt-11-1377-2018.

Brooks, H. E., C. A. Doswell III, and M. P. Kay, 2003: Climatological estimates of local daily tornado probability for the United States. *Wea. Forecasting*, **18**, 626–640, https://doi.org/10.1175/1520-0434(2003)018<0626:CEOLDT>2.0.CO;2.

Chandrasekar, V., W. A. Cooper, and V. N. Bringi, 1988: Axis ratios and oscillations of raindrops. *J. Atmos. Sci.*, **45**, 1323–1333, https://doi.org/10.1175/1520-0469(1988)045<1323:ARAOOR>2.0.CO;2.

Chowdhury, M. N., F. Y. Testik, M. C. Hornack, and A. A. Khan, 2016: Free fall of water drops in laboratory rainfall simulations. *Atmos. Res.*, **168**, 158–168, https://doi.org/10.1016/j.atmosres.2015.08.024.

Das, S. K., S. Simon, Y. K. Kolte, U. V. M. Krishna, S. M. Deshpande, and A. Hazra, 2020: Investigation of raindrops fall velocity during different monsoon seasons over the western Ghats, India. *Earth Space Sci.*, **7**, e2019EA000956, https://doi.org/10.1029/2019EA000956.

Davidson, P. A., 2015: *Turbulence: An Introduction for Scientists and Engineers.* Oxford University Press, 647 pp.

Dingle, N., and Y. Lee, 1972: Terminal fallspeeds of raindrops. *J. Appl. Meteor.*, **11**, 877–879, https://doi.org/10.1175/1520-0450(1972)011<0877:TFOR>2.0.CO;2.

Foote, G. B., and P. S. Du Toit, 1969: Terminal velocity of raindrops aloft. *J. Appl. Meteor.*, **8**, 249–253, https://doi.org/10.1175/1520-0450(1969)008<0249:TVORA>2.0.CO;2.

Green, A. W., 1975: An approximation for the shapes of large raindrops. *J. Appl. Meteor.*, **14**, 1578–1583, https://doi.org/10.1175/1520-0450(1975)014<1578:AAFTSO>2.0.CO;2.

Gunn, R., and G. D. Kinzer, 1949: The terminal velocity of fall for water droplets in stagnant air. *J. Meteor.*, **6**, 243–248, https://doi.org/10.1175/1520-0469(1949)006<0243:TTVOFF>2.0.CO;2.

Huang, G. J., V. N. Bringi, and M. Thurai, 2008: Orientation angle distributions of drops after an 80-m fall using a 2D video disdrometer. *J. Atmos. Oceanic Technol.*, **25**, 1717–1723, https://doi.org/10.1175/2008JTECHA1075.1.

Larsen, M. L., A. B. Kostinski, and A. R. Jameson, 2014: Further evidence for superterminal raindrops. *Geophys. Res. Lett.*, **41**, 6914–6918, https://doi.org/10.1002/2014GL061397.

Marzuki, W. L. Randeu, T. Kozu, T. Shimomai, H. Hashiguchi, and M. Schönhuber, 2013: Raindrop axis ratios, fall velocities and size distribution over Sumatra from 2D-video disdrometer measurement. *Atmos. Res.*, **119**, 23–37, https://doi.org/10.1016/j.atmosres.2011.08.006.

McDonald, J. E., 1954: The shape and aerodynamics of large raindrops. *J. Meteor.*, **11**, 478–494, https://doi.org/10.1175/1520-0469(1954)011<0478:TSAAOL>2.0.CO;2.

Montero-Martínez, G., and F. García-García, 2016: On the behaviour of raindrop fall speed due to wind. *Quart. J. Roy. Meteor. Soc.*, **142**, 2013–2020, https://doi.org/10.1002/qj.2794.

——, A. B. Kostinski, R. A. Shaw, and F. García-García, 2009: Do all raindrops fall at terminal speed? *Geophys. Res. Lett.*, **36**, L11818, https://doi.org/10.1029/2008GL037111.

Muñoz-Esparza, D., R. D. Sharman, and J. K. Lundquist, 2018: Turbulence dissipation rate in the atmospheric boundary layer: Observations and WRF mesoscale modeling during the XPIA field campaign. *Mon. Wea. Rev.*, **146**, 351–371, https://doi.org/10.1175/MWR-D-17-0186.1.

NOAA, 2020: Storm Event Database. National Centers for Environmental Information, accessed 9 May 2022, https://www.ncdc.noaa.gov/stormevents/eventdetails.jsp?id=891257.

——, 2022: Radar Data, version 3.1.0. National Centers for Environmental Information, accessed 9 May 2022, https://www.ncei.noaa.gov/maps/radar/.

OTT-Hydromet, 2016: Operating instructions precipitation gauge OTT Pluvio$^2$ L. 60 pp., https://images.otthydromet.com/asset-get.download.jsa?code=299718.

——, 2017: Operating instructions present weather sensor OTT Parsivel2. 52 pp., https://www.ott.com/download/operating-instructions-present-weather-sensor-ott-parsivel2-with-screen-heating-1/.

Pei, B., F. Y. Testik, and M. Gebremichael, 2014: Impacts of raindrop fall velocity and axis ratio errors on dual-polarization radar rainfall estimation. *J. Hydrometeor.*, **15**, 1849–1861, https://doi.org/10.1175/JHM-D-13-0201.1.

Piper, M., and J. K. Lundquist, 2004: Surface layer turbulence measurements during a frontal passage. *J. Atmos. Sci.*, **61**, 1768–1780, https://doi.org/10.1175/1520-0469(2004)061<1768:SLTMDA>2.0.CO;2.

Pollock, M. D., and Coauthors, 2018: Quantifying and mitigating wind-induced undercatch in rainfall measurements. *Water Resour. Res.*, **54**, 3863–3875, https://doi.org/10.1029/2017WR022421.

Pruppacher, H. R., and K. V. Beard, 1970: A wind tunnel investigation of the internal circulation and shape of water drops falling at terminal velocity in air. *Quart. J. Roy. Meteor. Soc.*, **96**, 247–256, https://doi.org/10.1002/qj.49709640807.

——, and R. L. Pitter, 1971: A semi-empirical determination of the shape of cloud and rain drops. *J. Atmos. Sci.*, **28**, 86–94, https://doi.org/10.1175/1520-0469(1971)028<0086:ASEDOT>2.0.CO;2.

Rahman, K., and F. Y. Testik, 2020: Shapes and fall speeds of freezing and frozen raindrops. *J. Hydrometeor.*, **21**, 1311–1331, https://doi.org/10.1175/JHM-D-19-0204.1.

Sugioka, K. I., and S. Komori, 2007: Drag and lift forces acting on a spherical water droplet in homogeneous linear shear air flow. *J. Fluid Mech.*, **570**, 155–175, https://doi.org/10.1017/S0022112006003065.

Suh, Y., and C. Lee, 2013: A numerical method for the calculation of drag and lift of a deformable droplet in shear flow. *J. Comput. Phys.*, **241**, 35–57, https://doi.org/10.1016/j.jcp.2013.01.034.

Suomi, I., and T. Vihma, 2018: Wind gust measurement techniques—From traditional anemometry to new possibilities. *Sensors*, **18**, 1300, https://doi.org/10.3390/s18041300.

Testik, F. Y., and A. P. Barros, 2007: Toward elucidating the microstructure of warm rainfall: A survey. *Rev. Geophys.*, **45**, RG2003, https://doi.org/10.1029/2005RG000182.

——, and M. Gebremichael, Eds., 2010: *Rainfall: State of the Science. Geophys. Monogr.*, Vol. 191, Amer. Geophys. Union, 287 pp.

——, and M. K. Rahman, 2016: High-speed optical disdrometer for rainfall microphysical observations. *J. Atmos. Oceanic Technol.*, **33**, 231–243, https://doi.org/10.1175/JTECH-D-15-0098.1.

——, and ——, 2017: First in situ observations of binary raindrop collisions. *Geophys. Res. Lett.*, **44**, 1175–1181, https://doi.org/10.1002/2017GL072516.

——, A. P. Barros, and L. F. Bliven, 2006: Field observations of multimode raindrop oscillations by high-speed imaging. *J. Atmos. Sci.*, **63**, 2663–2668, https://doi.org/10.1175/JAS3773.1.

Thompson, R. L., 1998: Eta model storm-relative winds associated with tornadic and nontornadic supercells. *Wea. Forecasting*,

**13**, 125–137, https://doi.org/10.1175/1520-0434(1998)013<0125:EMSRWA>2.0.CO;2.

Thurai, M., and V. N. Bringi, 2005: Drop axis ratios from a 2D video disdrometer. *J. Atmos. Oceanic Technol.*, **22**, 966–978, https://doi.org/10.1175/JTECH1767.1.

——, and V. Bringi, 2009: Shapes and orientations of raindrops from 2D-video disdrometer, polarimetric radar and a wind-tunnel study. *Third European Conf. on Antennas and Propagation*, Berlin, Germany, IEEE, 3438–3442, https://ieeexplore.ieee.org/document/5068335.

——, G. J. Huang, V. N. Bringi, W. L. Randeu, and M. Schönhuber, 2007: Drop shapes, model comparisons, and calculations of polarimetric radar parameters in rain. *J. Atmos. Oceanic Technol.*, **24**, 1019–1032, https://doi.org/10.1175/JTECH2051.1.

——, W. A. Petersen, A. Tokay, C. Schultz, and P. Gatlin, 2011: Drop size distribution comparisons between Parsivel and 2-D video disdrometers. *Adv. Geosci.*, **30**, 3–9, https://doi.org/10.5194/adgeo-30-3-2011.

——, V. N. Bringi, W. A. Petersen, and P. N. Gatlin, 2013: Drop shapes and fall speeds in rain: Two contrasting examples. *J. Appl. Meteor. Climatol.*, **52**, 2567–2581, https://doi.org/10.1175/JAMC-D-12-085.1.

Tokay, A., and K. V. Beard, 1996: A field study of raindrop oscillations. Part I: Observation of size spectra and evaluation of oscillation causes. *J. Appl. Meteor.*, **35**, 1671–1687, https://doi.org/10.1175/1520-0450(1996)035<1671:AFSORO>2.0.CO;2.

Vickers, D., and L. Mahrt, 1997: Quality control and flux sampling problems for tower and aircraft data. *J. Atmos. Oceanic Technol.*, **14**, 512–526, https://doi.org/10.1175/1520-0426(1997)014<0512:QCAFSP>2.0.CO;2.

Wang, P. K., and H. R. Pruppacher, 1977: Acceleration to terminal velocity of cloud and raindrops. *J. Appl. Meteor.*, **16**, 275–280, https://doi.org/10.1175/1520-0450(1977)016<0275:ATTVOC>2.0.CO;2.

Wilczak, J. M., S. P. Oncley, and S. A. Stage, 2001: Sonic anemometer tilt correction algorithms. *Bound.-Layer Meteor.*, **99**, 127–150, https://doi.org/10.1023/A:1018966204465.

Wobus, H. B., F. W. Murray, and L. R. Koenig, 1971: Calculation of the terminal velocity of water drops. *J. Appl. Meteor.*, **10**, 751–754, https://doi.org/10.1175/1520-0450(1971)010<0751:COTTVO>2.0.CO;2.